IMPACT CRATERING THEORY AND MODELING FOR THE DEEP IMPACT MISSION: FROM MISSION PLANNING TO DATA ANALYSIS

JAMES E. RICHARDSON[1,*], H. JAY MELOSH[1], NATASHA A. ARTEMEIVA[2]
and ELISABETTA PIERAZZO[3]

[1]*Lunar and Planetary Laboratory, University of Arizona, Tucson, AZ, U.S.A.*
[2]*Institute for the Dynamics of the Geospheres, Moscow, Russia*
[3]*Planetary Science Institute, Tucson, AZ, U.S.A.*
*(*Author for correspondence; E-mail: jrich@lpl.arizona.edu)*

Abstract. The cratering event produced by the Deep Impact mission is a unique experimental opportunity, beyond the capability of Earth-based laboratories with regard to the impacting energy, target material, space environment, and extremely low-gravity field. Consequently, impact cratering theory and modeling play an important role in this mission, from initial inception to final data analysis. Experimentally derived impact cratering scaling laws provide us with our best estimates for the crater diameter, depth, and formation time: critical in the mission planning stage for producing the flight plan and instrument specifications. Cratering theory has strongly influenced the impactor design, producing a probe that should produce the largest possible crater on the surface of Tempel 1 under a wide range of scenarios. Numerical hydrocode modeling allows us to estimate the volume and thermodynamic characteristics of the material vaporized in the early stages of the impact. Hydrocode modeling will also aid us in understanding the observed crater excavation process, especially in the area of impacts into porous materials. Finally, experimentally derived ejecta scaling laws and modeling provide us with a means to predict and analyze the observed behavior of the material launched from the comet during crater excavation, and may provide us with a unique means of estimating the magnitude of the comet's gravity field and by extension the mass and density of comet Tempel 1.

1. The Inception of Deep Impact

The idea of impacting a space probe into a small solar system body in order to investigate its composition and structure has its beginnings with a 1994 JPL concept study. Shortly thereafter, the Deep Impact mission was conceived in the fall of 1995, when Mike Belton met with Jay Melosh at the Lunar and Planetary Laboratory of the University of Arizona and asked the simple question "how large a crater would be produced by the impact of a 500 kg spacecraft at 10 km/s on a comet?" A quick estimate using the Schmidt–Holsapple scaling law gave a rough estimate of about 100 m diameter (Holsapple and Schmidt, 1982). Belton realized that this would excavate material from a substantial depth below the surface of the comet and that his idea of using an impact to probe the comet's interior made sense. This confirmation

expanded into the assembly of a science team and writing assignments for the first round of the Deep Impact proposal (which proposed Phaeton, not Tempel 1, as a target) in of June 1996.

As this project evolved, we were always painfully aware of the difficulty of making exact predictions of crater size on an almost entirely unknown target. No one then knew (nor yet knows) the density of a comet. Estimates for the density of Halley range from 0.03 to 4.9 g/cm^3 (Peale, 1989). Is the surface material of a comet inert like sand or will it release large amounts of volatile gases when it is struck and heated? Is the surface material strong like rock or as weak as the 100 Pa strength inferred for Comet SL9 (Scotti and Melosh, 1993)? Precise estimates of the size of the crater and the course of excavation depend on answers to these unknowns. In the end, we decided that the experiment itself must answer these questions: We would try, for the first time, to probe a comet by direct impact and deduce its mechanical properties from the response.

Although we remain very uncertain about what the Deep Impact experiment will eventually show, we have nevertheless tried to do the best job we could in predicting the outcome. Fortune, after all, favors the prepared mind. This paper represents our current best attempts to understand what we can expect to see when the 360 kg Deep Impact impactor strikes Tempel 1 at 10.2 km/s in early July 2005.

2. Scaling Relations for Crater Diameter

In one respect, our understanding of the Deep Impact cratering event is much better constrained than that of the multi-kilometer scale impact craters observed on the Earth and other moons and planets. Unlike the large craters that form a major part of the landscapes of most airless bodies, the relatively small Deep Impact crater is a good match to our ability to compute or experimentally model such impacts.

The formation of an impact crater does not involve any new physics. The impact and the subsequent growth of the crater are governed by a set of classical differential equations known as the Navier–Stokes equations, supplemented by an equation of state that describes the thermodynamic properties and constitutive equations that describe the strength of materials (see Melosh, 1989 for a review of cratering mechanics). The Navier–Stokes equations express the conservation of mass, energy and momentum. The "equation of state" relates the pressure in all materials and mixtures of materials to their densities and internal energies. The constitutive equations define a material model that links shear stresses and strains. The principal uncertainty in using these equations is the equation of state and material model. These relations are not well known for most natural materials. However, the equations themselves offer some hope for a simple solution. As in many such equations, they posses several "invariances:" changes of some variable that leaves the overall equation unchanged. If gravity or rate-dependent strength is not involved (which, as we will see, may be too drastic a simplification in practice), one of the principal

invariances is a coordinated change of size and time. Thus, a 1 mm projectile striking a target at 10 km/s will yield the same result as a 1 m projectile striking at the same speed, provided all distances are scaled by the same ratio of 1,000 = 1 m/1 mm and all times are multiplied by the same factor. Thus, if the 1 mm projectile makes a crater 6 cm in diameter in 300 ms, the 1 m projectile will create a 60 m diameter crater in 300 s. In this scaling, velocities, densities and strengths are unchanged. Thus, the target from which the problem is scaled must be the same material as the actual target.

This simple scaling invariance thus opens the door to detailed experimental study of the Deep Impact crater, providing we can find close matches to the actual material of a comet and achieve velocities similar to that of the Deep Impact collision. In fact, laboratory studies using two-stage light gas guns are limited to about 6–8 km/s, but this is not very far from the actual conditions. Schultz and Ernst (this volume) describe a detailed laboratory simulation approach using just this correspondence. The main factors that spoil this rosy picture are (1) target materials that posses a rate-dependent material strength, and (2) the Earth's gravity. Although many target materials do not have this first problem, rate dependence is observed for carbonates (Larson, 1977) and other materials, especially for tensile failure, where a strong rate dependence is expected (Melosh *et al.*, 1992), so caution is needed here. If gravity is important in limiting the crater's growth (and, depending on the strength of the material in the target, it may or may not be), then this simple invariance does not hold. Gravity is a function of $(\text{distance})/(\text{time})^2$; so, for a strictly correct comparison between the laboratory and the actual event, the acceleration of gravity must be scaled as the inverse of the distance or time ratio. Thus, the 1 mm projectile in a terrestrial gravity field corresponds to a 1 m projectile in a gravity field of 1/1,000 of Earth's surface gravity. This is certainly a step in the right direction for the Deep Impact event, in which the surface gravity on Tempel 1 may be only be 0.0008 m/s^2, but it actually goes about a factor 10 too far! To simulate the comet impact correctly under Earth gravity we really need a projectile about $80\,\mu\text{m}$ in diameter, made of the same materials as the Deep Impact impactor and striking a target of the same composition as the comet at 10.2 km/s. Even the grain size of the Earth simulant target must be reduced by the same factor of 8×10^{-5} from the grain size in the comet. This is a pretty tall order for experimental studies and may require the numerical methods described later to make serious progress, although any numerical computation must, of course, be checked by experimental findings under all possible circumstances.

Although it is often difficult to satisfy the requirements of the exact space/time/material invariance, an approximate form of invariance has been recognized in impacts and explosions. This invariance ultimately stems from the fact that the final crater is much larger than the projectile, so that projectile-specific properties such as diameter, shape, composition, angle of impact, etc., do not affect the final outcome. Only a single-dimensional parameter, the "coupling parameter" that depends on the projectile's total energy and momentum may affect the size

and shape of the end result (Holsapple and Schmidt, 1982). When this is the case, a number of "scaling relations" can be derived that link impacts at different sizes, velocities and gravitational accelerations. Such scaling relations take the form of power laws relating dimensionless combinations of quantities describing the projectile and final crater:

$$\pi_D = C_D \pi_2^{-\beta},\tag{1}$$

where π_D is a dimensionless measure of crater diameter,

$$\pi_D = D\left(\frac{\rho_t}{m}\right)^{1/3},\tag{2}$$

in which D is the transient crater diameter measured at the level of the pre-impact surface (the "apparent" diameter), ρ_t the target density, m the projectile mass, and π_2 the inverse of the Froude number,

$$\pi_2 = \frac{1.61gL}{v_i^2},\tag{3}$$

where g is the surface gravity, L the projectile diameter and v_i the impact velocity. C_D and β are constants that are determined empirically. These constants depend on the nature of the target material, in particular on its porosity or coefficient of internal friction. Table I lists values of these coefficients determined from a suite of experiments by Schmidt and Housen (1987). Note that such scaling laws apply only to the final state of the crater. Early-time phenomena such as melt or vapor production depend on the details of the impactor and thus cannot be predicted from a scheme of this type.

In most previous planetary studies, the large craters that are of principal interest form at values of π_2 much in excess of what can be measured in the laboratory, making extrapolation to large values of π_2 necessary. In contrast, the Deep Impact crater will occur at a value of π_2 of about 10^{-11}, much *smaller* than has been observed in laboratory experiments, where it usually ranges from 10^{-5} to about 5×10^{-10}. Little data have been reported for high-velocity impacts into dry sand and water in which π_2 ranged down to about 10^{-10} (Schmidt and Housen, 1987). In this case, we must extrapolate π_2 to the opposite extreme from most previous

TABLE I

Experimental parameters for diameter scaling law (Schmidt and Housen, 1987).

Target material	C_D	β
Water	1.88	0.22
Loose sand	1.54	0.165
Competent rock or saturated soil	1.6	0.22

TABLE II

Diameter estimates for the Deep Impact crater from three different scaling laws (Melosh 1989).

Scaling method	Diameter (m)
Yield scaling	63.5
Pi scaling	60.4 for loose sand
	250 for competent rock
Gault scaling	65.7

Impact conditions: projectile diameter: 1 m; projectile density: 0.46 g/cm^3; impact velocity: 10.2 km/s; angle from horizontal: 90°; target density: 1.0 g/cm^3; acceleration of gravity: 0.0008 m/s^2. The formation time is 350 s.

studies. Table II illustrates the range in uncertainty in crater diameter predictions using scaling relations from a variety of sources. The expected range in diameter for a gravity-dominated crater is thus 60–250 m, depending on the nature of the target (loose sand versus competent rock). The reader may be surprised that the crater diameter in "competent rock" is larger than that of "loose sand". This is a simple consequence of the more rapid attenuation of shock waves in loose materials. This relationship has been observed in a large number of impact experiments and numerical simulations (see, e.g., Figure 7.3 of Melosh, 1989).

When material strength, not gravity, finally halts the crater growth, similar power-law scaling relations can be constructed in which the important dimensionless variable is not π_2 but a combination depending on some measure of strength, Y:

$$\pi_3 = \frac{Y}{\rho_p v_i^2}, \tag{4}$$

where ρ_p is the density of the projectile (Holsapple and Schmidt, 1982). Although implementation of this sort of relationship appears simple, at the moment it is unclear how to implement strength scaling. The problem is that it is uncertain what the strength measure Y really is: One could use either tensile strength or crushing strength, but the two often differ by an order of magnitude.

The entire concept of what is meant by "strength" in impact cratering is presently somewhat fuzzy. Modern theories of dynamic fracture indicate that the actual failure strength should be strongly rate dependent (Grady and Kipp, 1987), a factor not considered in the derivation of the original strength scaling relations. Furthermore, numerical computations indicate that the strength of the material surrounding an impact is often strongly degraded by the shock wave long before the excavation flow clears the material out of the crater interior (Croft, 1981; Asphaug and Melosh, 1993; Nolan *et al.*, 1996). This pre-excavation fracture appears to depend strongly on crater size as well as intrinsic strength, being more important in small gravitational

fields than in large ones. At a much larger scale, the collapse of multi-kilometer craters clearly requires some form of extreme strength degradation mechanism to match observations with theory (Melosh and Ivanov, 1999).

Another area of uncertainty is the effect of the special aspects of a cometary surface on crater growth. We presently have very little experience with high-velocity impacts on highly volatile targets in which a significant amount of material may be melted or vaporized, although a number of low-velocity analog experiments have been performed (Schultz *et al.*, 1992). The expansion of a large quantity of volatile material can only be expected to increase the crater size by pushing more material away from the impact site. Some experiments with highly volatile cadmium projectiles and targets have been performed (Poorman and Piekutowski, 1995), but the relevance of these experiments to the surface of a comet with an unknown suite of ices with unknown abundances is unclear.

Comet surfaces are also expected to be highly porous, with estimates of porosity of the outer crust ranging from essentially zero to more than 50% (Sagdeev *et al.*, 1988). In the extreme limit of low porosity, the impacting spacecraft might simply pass through the comet. We do not really expect this to happen. The best current estimate of cometary density, derived from the tidal breakup of SL9, suggests that is in the neighborhood of 0.5 g/cm^3 (Asphaug and Benz, 1994), which is certainly high enough to prevent the spacecraft from penetrating the entire object.

The presence of a certain amount of porosity is actually advantageous to producing a large crater. It has long been known that the excavation efficiency of a buried explosion is a strong function of the depth of burial (Nordyke, 1962). Experience with both high explosives and nuclear detonations indicates that the scaled crater diameter, $D/W^{1/3}$, where W is the energy release, increases with scaled depth of burial, $h/W^{1/3}$, until the "optimum depth of burial" is reached at about 0.003 m/J$^{1/3}$. Explosions at greater depths produce smaller craters, until at depths in excess of 0.009 m/J$^{1/3}$ crater formation is entirely suppressed. For the Deep Impact spacecraft, which delivers about 1.9×10^{10} J to the comet, this depth is about 8 m. The penetration depth of a projectile is given roughly by $d = L\sqrt{\rho_p/\rho_t}$, which is based on simple momentum conservation (Melosh, 1989). For a projectile 1 m in diameter and average density $\rho_p = 0.46$ g/cm^3 impacting a target of similar density, the penetration depth is only 1 m, well short of the optimum depth. This accords with general experience: Impact craters are generally considered similar to explosions buried at shallow depth (Holsapple, 1980). Thus, within wide limits a lower target density permits the projectile to penetrate deeper and creates a larger crater. Only if the comet density were lower than 0.007 g/cm^3 (which gives a penetration depth greater than 8 m, based on the penetration formula given earlier) would the crater size decrease as a result of excessively deep penetration. Nevertheless, some concern has been expressed about the possibility that a high-density projectile might penetrate so deeply that crater excavation is suppressed. This concern has partly driven the design of the Impactor Spacecraft, as discussed in the next section.

3. Cratering Constraints on the Impactor Spacecraft Design

Some of the unique features of the Deep Impact mission generated strong constraints on the design of the Impactor Spacecraft. The mass and shape of the Impactor were optimized to create the largest possible crater under the widest possible range of circumstances. Moreover, because we hope to determine the comet's composition from spectral emissions from the material vaporized by the impact, constraints arose on the elemental composition of the Impactor.

The Impactor itself is a roughly cylindrical spacecraft about 1 m in diameter and 1 m long (Figure 1). In addition to the impacting mass itself, it contains a small propulsion system, guidance, communications, and imaging systems. Because it must fly through the coma of an active Tempel 1 before impact, a three-plate
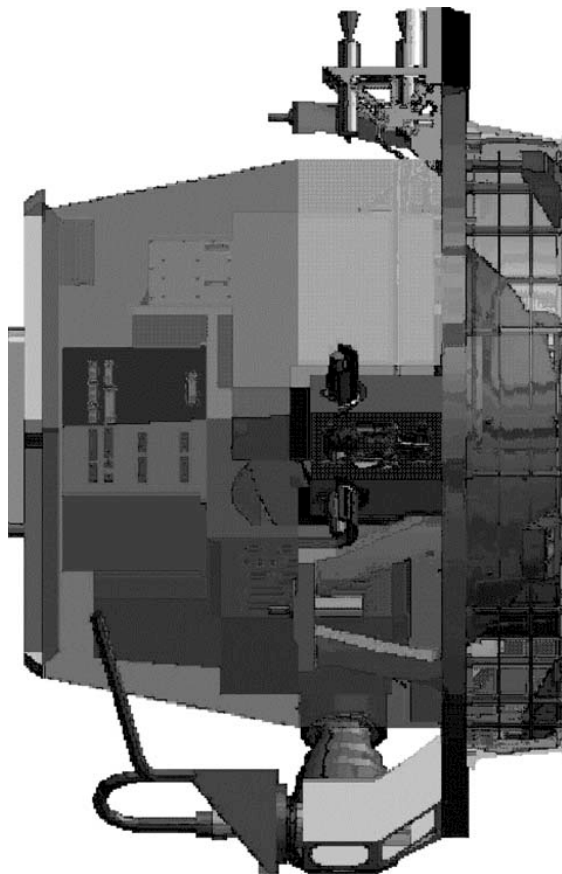

Figure 1. Schematic view of the Deep Impact Impactor Spacecraft.

Whipple shield protects its forward end. We expect to be able to survive impacts by 1 g coma dust particles at the approach velocity of 10.2 km/s. Only about 1/3 of the total mass could be devoted to inert impact mass. An early decision was to make this material from the metal copper. Copper also possesses well-defined lines that should not mask emissions of other species of geochemical interest (assuming that it is in the vapor phase, not in the form of incandescent droplets). In addition to the desirable thermal and mechanical properties of copper, it is an element in which few geochemists have expressed a serious interest. The fact that the emissions from the copper vapor, from the projectile will overwhelm the signature of any copper in the target was thus not considered a drawback.

The abundances of elements of more geochemical interest than copper, however, generated a unique set of constraints on the impactor. Assuming that the impact will vaporize a mass of target roughly equal to the mass of the impactor, we estimated the probable mass of a suite of elements likely to be vaporized from the target (Table III), based on abundances of elements in the lunar soil (Heiken *et al.*, 1991), Type I carbonaceous chondrites (Taylor, 1982), and in Comet Halley dust (Jessberger, 1999). We then required that the impactor not contain more than 20% of these strategic elements. This limit was further lowered for elements that have strong emission lines that might mask those of other elements of interest. Table III

TABLE III

Estimated composition of vaporized comet crust vs. Impactor Spacecraft.

Element	Mass in DI vapor plume (kg)	Mass in DI Impactor Spacecraft (kg)
O	123	1.8
Na	2.8	a
Mg	49	1.0
Al	4.5	78.2
Si	55	0.4
K	0.3	a
Ca	4.9	a
Ti	0.23	24.9
Mn	1.2	a
Fe	95.2	14.4
Co	0.1	0.0
Ni	0.3	2.0
Cu	0.006	178.1

Masses are based on a devolatilized composition similar to Type I carbonaceous chondrites (Taylor, 1982). Mass vaporized: 350 kg.
[a]These elements were not reported separately. The total mass of unreported elements was 4.4 kg.

also lists the final composition of the projectile (Alice Phinney, 2004, personal communication) for comparison.

The precise distribution of the inert mass generated considerable discussion during the design phase, executed by Alice Phinney and her team at Ball Aerospace, Inc. For structural reasons, the engineers initially wanted to put all of the copper in a thin disc-shaped plate about 1 m in diameter. However, because we are not certain that we will ever know the precise angle of impact, and because we expect that the outcome of the event will depend on whether the plate entered on edge or face-on, the science team wanted to put as much mass as possible into a sphere. In the end, a compromise was reached in which the leading end of the impactor was faced with a 1 m diameter copper disk of mass 15 kg on which is mounted a 0.64 m diameter spherical segment 0.16 m high. The plate and spherical segment are constructed from a stack of copper plates (Figure 2) in which numerous non-overlapping holes are milled, lowering the average density of the mass to 4.0 g/cm^3. The entire copper fore-body has a mass of 113 kg out of a total spacecraft mass (at impact) of 360 kg. This configuration has the advantage that, if the comet turns out to have a very low density, the broad extension of the plate and after-body will couple the spacecraft momentum gradually into the target. On the other hand, if the comet is very dense, the spherical segment alone will penetrate deeply while the remainder of the spacecraft is stripped away near the surface. In both cases, we will couple a large fraction of the impactor's kinetic energy deeply into the target.

The complicated structure of the spacecraft (and probably of the target) make it impossible to be confident about the validity of the simple scaling relations described earlier. In the final analysis, a coupled series of detailed numerical simulations and experimental studies will probably have to be carried out to resolve the details of the impact process.
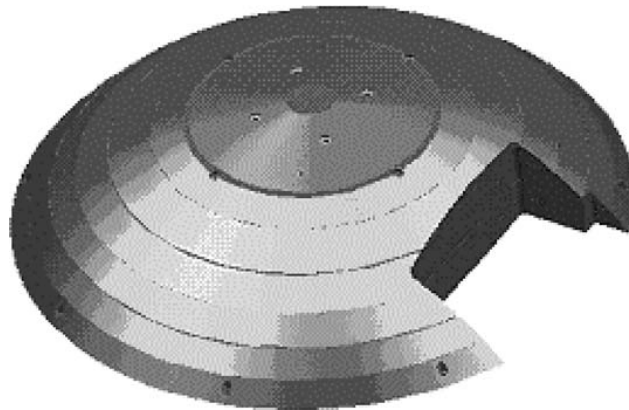

Figure 2. Forebody copper mass. Diameter 0.64 m, height of stack 0.16 m, mass 113 kg.

4. The Early Stages of Impact and Vapor Plume Formation

One of the many unique features of this mission is the ability to determine the composition of the comet's crust by observing the vaporized material produced by the impact in its earliest stages. As discussed earlier, this vapor plume will consist of a mixture of impactor and comet material, and in addition to avoiding elements of interest and cataloguing exactly what is in the impactor (Table III) it can be useful to model the evolution of the vapor plume to understand how its observed composition and thermodynamics will change over time. The earliest stages of contact of the Deep Impact spacecraft with Tempel 1 can be simulated either experimentally (Shultz and Ernst, this volume), or theoretically using a computer code to solve the equations describing the projectile and target, so far as they are known. The penetration phase of this impact is short: about 0.1 ms for the 1 m projectile to fully contact the target at 10.2 km/s. Nevertheless, we can get a rough idea of the early events using a modern numerical hydrocode (Anderson, 1987).

We performed high-resolution three-dimensional (3D) hydrocode simulations of the early stages of impact cratering events using the hydrocode SOVA (Shuvalov, 1999) coupled to tabular versions of the ANEOS equations of state (Thompson and Lauson, 1972) for the materials of interest. The objective of this study is to investigate impactor penetration, and the development and evolution of the expansion plume at early times.

SOVA (Shuvalov, 1999) is a two-step Eulerian code developed at the Institute for Dynamics of Geospheres (Russia) that can model multidimensional, multi-material, large deformation, strong shock wave physics. It is based on the same principles utilized in the well-known hydrocode CTH (McGlaun *et al.*, 1990), developed at the Sandia National Laboratories (Albuquerque, NM). In particular, care has been used in SOVA to develop a more appropriate formalism for the simultaneous conservation of energy and momentum. We use the code in 3D geometry; in this case, it is common practice to use bilateral symmetry, which will allow us to model only the positive half-space originating at the impact plane (the plane perpendicular to the target defined by the impact direction), thus significantly reducing the rather large mesh size (and accompanying computational requirements) needed for the simulation. Three-dimensional benchmark tests have shown that SOVA produces shock melting and vaporization patterns and volumes comparable to the well-known CTH (Pierazzo *et al.*, 2001; Artemieva and Ivanov, 2001). Tabular equations of state were constructed using a revised version of the ANEOS code (Thompson and Lauson, 1972; Melosh, 2000). The availability of reliable, wide range equations of state relating thermodynamic parameters of materials, such as pressure, density and temperature, is vitally important for numerical simulations. By using different physical treatments in different domains of validity, ANEOS provides a thermodynamically consistent equation of state whose validity extends over a wide range of temperatures and pressures. ANEOS also offers a limited treatment of material's phase changes. As a result, this code can model the thermodynamic evolution of a material

well beyond the initial shock stage, accounting for melting and vaporization, and providing consistent estimates of material's energies and entropies.

In the simulations, we tried to simulate the Deep Impact copper projectile as closely as possible. The impactor consists of a copper cylinder 0.4 m in radius and 0.8 m in height, with an average density of 660 kg/m^3, with a leading face made of a combination of two solid copper plates (density of 8,400 kg/m^3), one 0.4 m in radius followed by another 0.2 m in radius, with thickness of 2 cm each. The total mass of the projectile is 370 kg, with 120 kg concentrated on the solid leading face. The impact velocity is 10.2 km/s (as expected for the Deep Impact projectile). Our simulations model impact angles of 90° from the surface. At this early stage in the calculation, the acceleration of gravity is unimportant. The spatial resolution is 40 cells per projectile radius in the initial stage of penetration (i.e., the total thickness of the two solid plates on the leading edge spans four cells). Many believe that comets have a rocky surface crust few meters thick covering an ice-rich interior (Brandt and Chapman, 2004). We used serpentine (hydrated olivine, similar to the composition of carbonaceous chondrites) to model the crustal material. Since the typical density of the surface crust is not known, we carried out exploratory runs for (a) fully dense serpentine (unrealistic case; $\rho_t = 2.55$ g/cm^3); (b) 50% porous serpentine ($\rho_t = 1.275$ g/cm^3); (c) 80% porous serpentine ($\rho_t = 0.51$ g/cm^3). For comparison, we also carried out a simulation of a 45° impact and same setup as case (b). Figure 3 shows the outputs for the various simulations 0.7 ms after impact. The material colors are graded according to density variations, while colors of the Lagrangian tracers in the target represent the maximum shock experienced by the material. Figure 3 shows that the density of the target material affects the evolution of the expansion plume: in the highly porous surface case, Figure 3C, the impactor penetrates deep into the target, allowing target vapor to emerge relatively free of copper contamination. For a denser target, Figure 3A and B, copper vapor emerges early, mixed with target vapor. In the case of the oblique impact Figure 3D, the copper vapor appears to envelope the vapor from the target. This occurs from the very early stages of the impact, as a result of the asymmetry in the impact event, as shown in Figure 4. Further study will investigate if the copper vapor opacity is high enough to significantly affect the identification of target material from the plume.

5. Hydrocode Modeling of Crater Excavation

Once the kinetic energy of the projectile has coupled into the target, the ensuing shock wave spreads out and initiates the excavation stage of cratering (e.g. Melosh, 1989). The shock wave first compresses, then releases the engulfed material to low pressure. In the process, this material is accelerated away from the impact site and eventually opens a crater as comet surface materials are both displaced further downward into the comet or ejected from the surface. The most visible part of this
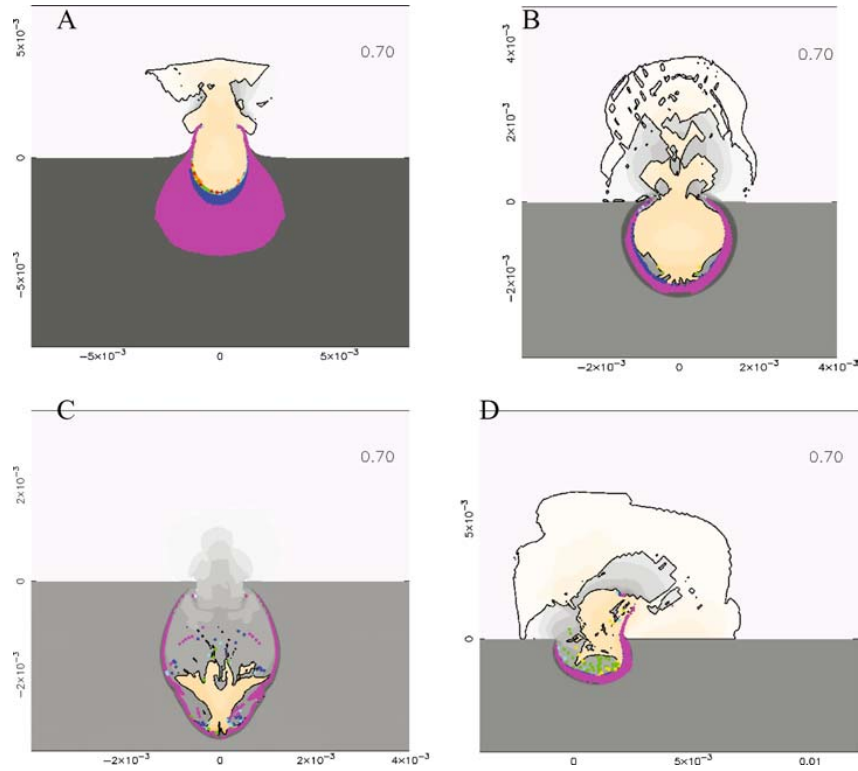
Figure 3. Impact simulation outputs 0.7 ms after impact for the various simulations: (A – *upper left*) fully dense serpentine ($\rho = 2.55$ g/cm^3); (B – *upper right*) 50% porous serpentine ($\rho = 1.275$ g/cm^3); (C – *lower left*) 80% porous serpentine ($\rho = 0.51$ g/cm^3); (D – *lower right*) 45° impact and same setup as (B). Material colors: gray: serpentine; yellow: copper impactor. Tracer colors represent target material shocked at various levels: yellow, 100–150 GPa; green, 50–100 GPa; cyan, 30–50 GPa; blue, 18–30 GPa; magenta, 5–18 GPa.

process is the ejecta plume, described in detail in the next section. The crater cavity itself is a consequence of both displacement and ejection.

Numerical modeling of impact crater excavation has now reached a high degree of sophistication (Collins *et al.*, 2004). Successful models have been created for a number of large terrestrial and extraterrestrial impact craters, and more are currently in progress. However, the Deep Impact crater presents a number of unique challenges. The principal one is the importance of treating porosity (Love *et al.*, 1993), dilatancy and strength in the comet crust. While we are not certain that the crust is highly porous, current best estimates of comet density strongly suggest that the volatile-depleted lag material we expect to find mantling the icy interior is probably an open granular aggregate of some kind, although opinion varies as to whether it is loose or sintered. The Stardust images of Comet Wild 2 showed
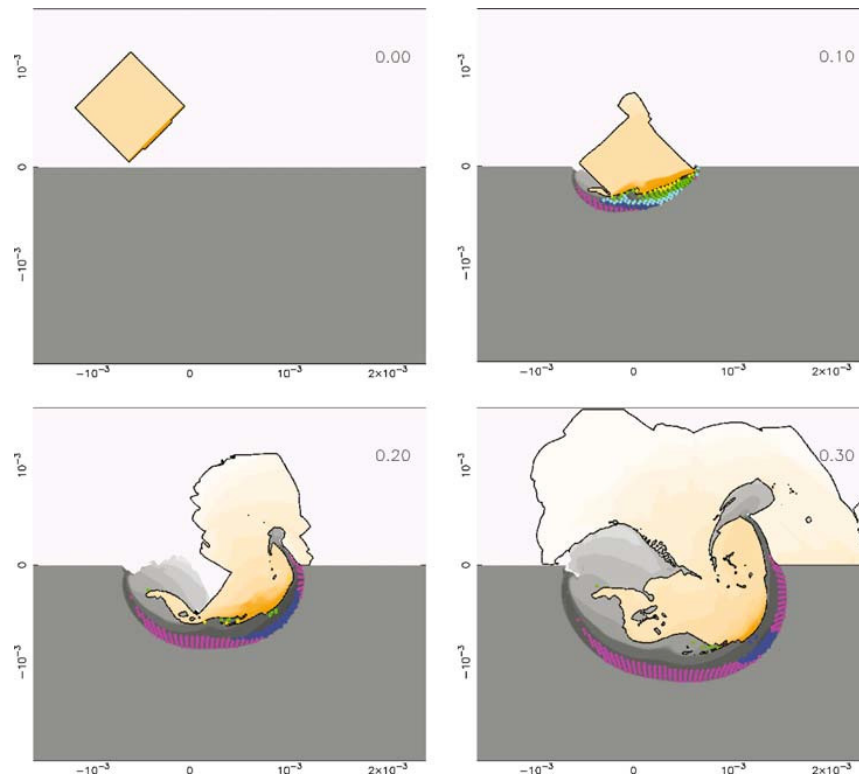
Figure 4. Impact simulation outputs for the 45° impact simulation (case D in Figure 3) in the early stages of impact, and shown for time after impact of: (*upper left*) 0 ms, (*upper right*) 0.1 ms, (*lower left*) 0.2 ms, and (*lower right*) 0.3 ms. Material and tracer colors are the same as in Figure 3.

spectacular 100 m high vertical cliffs that require some cohesion (Brownlee *et al.*, 2004), although in the feeble gravitational field of the comet this strength may be no larger than 100 Pa. Although we have recently made substantial progress in introducing realistic strength models into hydrocodes (Collins *et al.*, 2004; Wünnemann and Ivanov, 2003), the addition of porosity is less advanced (Rubin *et al.*, 2000) and dilatancy still needs a great deal of development (Wroth and Bassett, 1983).

To date, there are no complete numerical simulations of the Deep Impact crater from initial contact to final excavation, in spite of attempts by workers such as the O'Keefe and Ahrens team at Caltech and David Crawford of Sandia National Laboratory. Work on this topic is presently progressing and some results may be obtained by the time of impact on Tempel 1. Because laboratory models cannot adequately simulate every aspect of the comet's surface, research of this type is a prime necessity for establishing a link between the observed crater and the mechanical properties of Tempel 1's surface.

6. Impact Ejecta Behavior

6.1. INTRODUCTION

One important aspect of the Deep Impact mission is analyzing the behavior of the impact ejecta produced by the crater excavation process. Following impact, individual ejecta particles are launched ballistically from the edge of the bowl of the expanding crater, and collectively these particles form an inverted, cone-shaped plume (or curtain) which also expands over time (Figure 5). The ballistic behavior
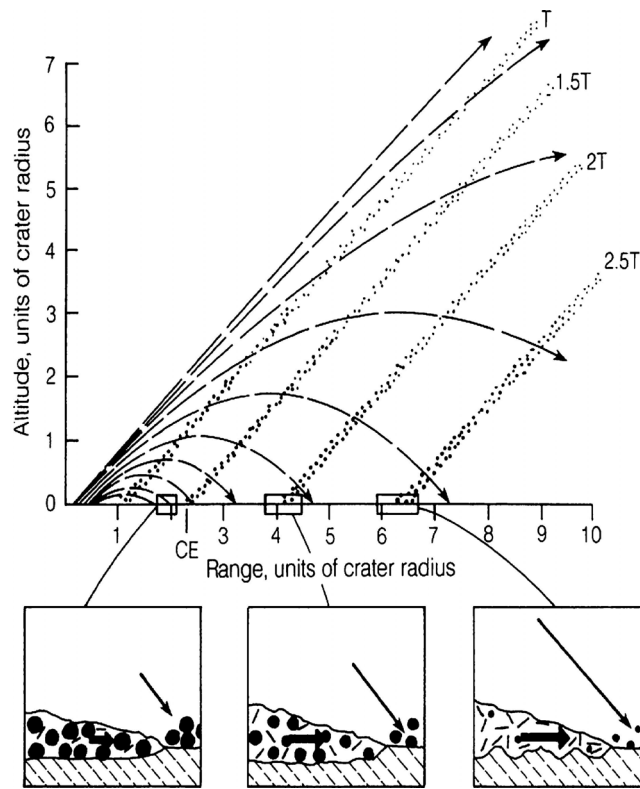
Figure 5. The debris ejected from an impact crater follows ballistic trajectories from its launch position within the transient crater (horizontal scale is in units of *R*). The innermost ejecta are launched first and travel fastest, following the steepest trajectories shown in the figure. Ejecta originating farther from the center are launched later and move more slowly, and fall nearer to the crater rim. Because of the relationship between the position, time, and velocity of ejection, the debris forms an inverted cone that sweeps outward across the target. This debris curtain (plume) is shown at four separate times during its flight, at 1, 1.5, 2, and 2.5 t_f, where t_f is the crater formation time. Figure reproduced from Melosh, 1989.

of the individual particles and the collective behavior of the ejecta plume are both heavily affected by the velocity and characteristics of the impactor (which we control); and target parameters such as the density, strength, porosity, and gravity field. By modeling the observed behavior of individual ejecta particles and the collective ejecta plume resulting from the mission, we hope to place constraints on these parameters.

6.2. IMPACT EJECTA SCALING LAWS

To model the impact ejecta behavior, we develop a revised set of crater growth, ejection time, and ejecta velocity scaling laws, based on the scaling laws described by Housen *et al.* (1983). The two relationships used here are based on gravity-dominated cratering in an experimental environment and are given by:

Crater formation time:

$$t_f = \frac{1}{2}\sqrt{\frac{2R}{g}}, \tag{5}$$

Ejecta velocity as a function of crater radius:

$$v_{ej} = C_e\left(\frac{r}{R}\right)^{-\varepsilon}, \tag{6}$$

where R is the gravity-dominated transient crater radius ($D/2$), r the crater radius as a function of time, g the surface gravitational acceleration, and ε is a material constant ranging from 1.8 for competent rock to 2.6 for quartz sand (Melosh, 1989). The coefficient of 1/2 in front of the crater formation time equation (Equation (5)) comes from an empirically derived value of 0.54 given by Melosh (1989).

We find the constant C_e by assuming that the crater rim advancement velocity must be equal to the horizontal component of the particle ejection velocity, such that the ejecta plume base and crater rim advance at the same rate. We take advantage of this by setting the particle ejection angle to a mean of $\theta = 45°$ above the horizon, which gives $v_{horizontal} = \sqrt{2}/2 v_{ej}$. Letting $v_{horizontal}$ equal the rim advancement speed produces:

$$\frac{\partial r}{\partial t} = \frac{\sqrt{2}}{2}C_e\left(\frac{r}{R}\right)^{-\varepsilon}. \tag{7}$$

Solving this differential equation such that r is allowed to move from $0 \rightarrow r$ while t moves from $0 \rightarrow t$, yields:

$$r = \left(\frac{\sqrt{2}}{2}(1+\varepsilon)C_e R^\varepsilon t\right)^{1/1+\varepsilon} \tag{8}$$

Letting $r = R$ and $t = t_f$ produces a crater formation time of:

$$t_f = \frac{\sqrt{2}R}{C_e(1+\varepsilon)}.$$

(9)

However, t_f is also given by Equation (2), allowing a solution for C_e to be found:

$$C_e = \frac{2\sqrt{Rg}}{1+\varepsilon}.$$

(10)

This gives the following two model equations, in addition to Equation (5):

Ejecta velocity as function of crater radius (replaces Equation (6))

$$v_{ej} = \frac{2\sqrt{Rg}}{1+\varepsilon}\left(\frac{r}{R}\right)^{-\varepsilon},$$

(11)

Particle ejection time as a function of rim position:

$$t_{ej} = \frac{\sqrt{2}r^{1+\varepsilon}}{2\sqrt{g}R^{(\varepsilon+1/2)}}.$$

(12)

We further modify Equation (11) to simulate late-stage ejection velocities more properly, when the crater radius is approaching its final value. In gravity-dominated cratering, the particle ejection (ballistic) velocity should go to zero as r goes to R, while Equation (11) instead goes to a constant (a weakness also described in Housen *et al.*, 1983). We correct this by subtracting a higher-order term, which has negligible effect throughout most of the excavation process, but which ramps the velocity expression to zero as the final (transient crater) rim is approached – essentially applying a mathematical bridge between known good behaviors. This gives the following equations.

Ejecta velocity as function of crater radius (replaces Equations (6) and (11)):

$$v_{ej} = \frac{2\sqrt{Rg}}{1+\varepsilon}\left(\frac{r}{R}\right)^{-\varepsilon} - \frac{2\sqrt{Rg}}{1+\varepsilon}\left(\frac{r}{R}\right)^{\lambda},$$

(13)

where the power λ is selected by the model user ($\lambda \approx 6$–10). Figure 6 shows a plot of ejection velocities produced from Equation (13), compared to experimentally derived values.

6.3. EJECTA PLUME TRACER MODEL

These scaling law equations are then applied to a dynamical simulation which models – *via* thousands of point tracer particles – the ejecta plume behavior, ejecta blanket placement, and impact crater area resulting from a specified impact on an irregularly shaped target body (similar to Geissler *et al.*, 1996). Figure 7 shows an example of one impact simulation, visualized in 3D polygon fashion. Placing the target body (shape-model) into a simple rotation state about one of its principal axes, the user then inputs an impact site and a set of projectile/target parameters.
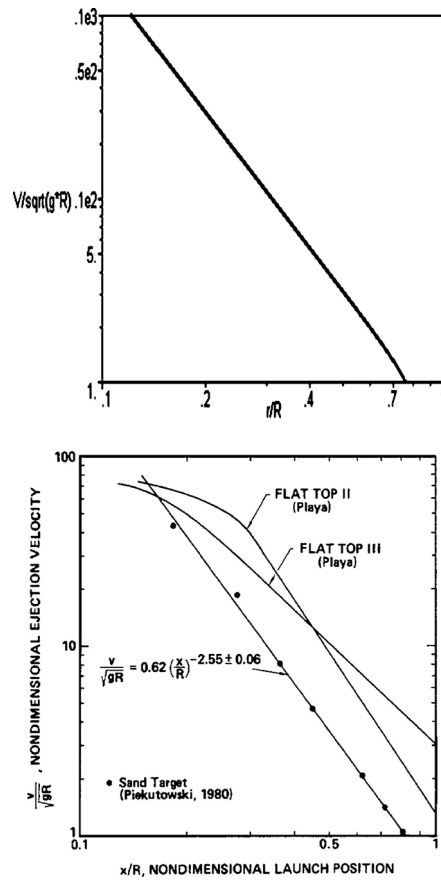
Figure 6. (A) Normalized (non-dimensional) ejecta velocities produced using Equation (9) as a function of the normalized radial position *r* within the transient crater of radius *R*. The values computed are for loose sand, with $\varepsilon = 2.44$ and a normalized equation coefficient of 0.58. (B) Experimentally measured ejecta velocities produced from large explosion craters and published in Figure 4 of Housen *et al.* (1983). The best model-experiment agreement corresponds to the lower sand target values.

From this information, the program places a circular transient crater area on the surface and populates this area with random tracer particles that have a spatial distribution such that each particle represents a roughly equal volume of ejecta. Once positioned, each particle is assigned an ejection time (Equation (12)), velocity (Equation (13)), and direction (radially outward at ejection angle θ above the horizon, discussed later), after which the simulation clock begins. While in flight, the gravitational acceleration from the irregular target body on each tracer particle is computed using the polygonized surface (polyhedron) gravity technique developed

Figure 7. A simulation showing the ejecta plume (*white tracer particles*), ejecta blanket (*yellow tracer particles*), and impact crater surface area (*shown in blue*) resulting from a small impact on an Eros-shaped target body having a 6-h rotation period about its principal *z*-axis. The top panel shows the state of the ejecta 6 min after the impact, using 2000 tracer particles to map its behavior. The ejecta plume is fully formed at this stage, with the slowest particles beginning to fall out near the crater rim. The bottom panel shows the state of the ejecta 6 h after the impact (one rotation), with most of the tracer particles landed again on the surface to form the ejecta blanket. This blanket is slightly asymmetrical, with more ejecta in the trailing direction (to the right) than in the leading direction.

by Werner (1994). The model tracks all tracer particles until they have either left the gravitational sphere of influence of the body (escaped) or landed again on the surface.

To properly model the ejection angle variations that occur over time in impact cratering experiments (Cintala *et al.*, 1999; Anderson *et al.*, 2003), we mimic the empirical data by allowing the particle ejection angle to drop from $\theta = 60$ to $30°$ as the crater rim (r) moves from 1 projectile diameter (its starting point) to the transient crater radius (R). This feature also causes the ejecta plume shape to change as a function of time, demonstrated in the Cintala *et al.* (1999) experiments and compared to the model in Figure 8. If a gravity-dominated cratering event occurs as a result of our impact on Tempel 1, the shape of the ejecta plume will provide a means for marking the end of the crater formation process (end of excavation flow) as the ejecta plume changes shape from concave during excavation, to straight at the transient crater rim (end of excavation), to convex during the post excavation (fall-out) stage.

In the event that the crater excavation is dominated by strength, we have added a target strength parameter (R_s) to the model, which cuts off crater growth and excavation flow when the inertial stress on the material reaches a user-assigned material yield stress (Y). This is determined by the equation (Melosh, 1989):

$$R_s = \frac{\rho_t v_{ej}^2}{Y}. \tag{14}$$

where ρ_t is the surface density. Unlike gravity-dominated excavation, in which the ejecta plume remains attached to the target surface throughout its formation and fall-out stages, in strength-dominated excavation the ejecta plume detaches completely from the target. In this case, the plume's bottom edge will follow a radial (with respect to the crater) ballistic path away from the edge of the truncated impact crater. While this form of cratering will give us a smaller final impact crater (and perhaps less chance of looking inside of the cavity), the ballistic path followed by the bottom edge of the ejecta plume (and perhaps some large late-ejected fragments) may provide us with our best opportunity for the determining magnitude of the comet's gravity field.

Collectively, the expansion rate of the ejecta plume (especially in a gravity-dominated event) can itself be used to gain a measure of the surface gravity field g, in part due to a g dependence in the particle ejection velocities (Equation (13)), but primarily due to the effect of gravity on the ballistic paths followed by the individual particles. Figure 9 shows the effect of varying the gravitational force (by varying the density of a constant volume model) on the ejecta plume base position and velocity as a function of time. If this form of plume behavior can be observed at high enough resolution for several minutes following the impact, then a surface gravity and comet mass can be estimated (albeit roughly), as well as obtaining an approximation for the comet's density by using the volume obtained from shape-modeling (Thomas, this volume).
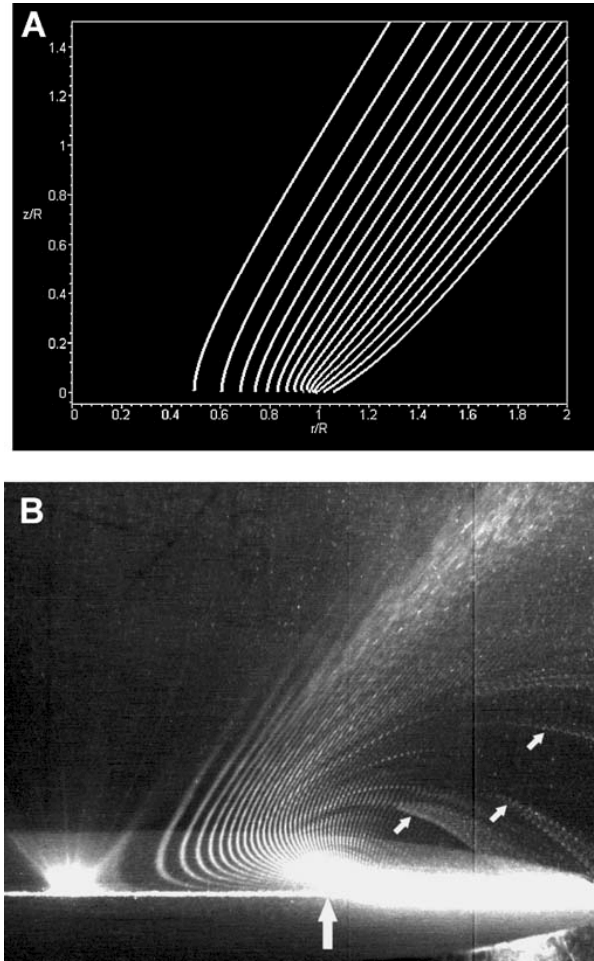
Figure 8. Ejecta plume profile comparisons between the ejecta plume model (A) and a small-scale cratering experiment (B) performed by Cintala *et al.* (1999) and based on their Figure 11, in which a 3.18 mm glass sphere was shot into fine-grained sand at 1.24 m/s to form an ∼4 cm diameter crater. The top panel shows both horizontal and vertical scales normalized to the transient crater radius *R*, while the bottom panel shows a large vertical arrow at the transient crater rim (small arrows point out the ballistic paths of three individual ejecta particles). The plume profiles in the top panel are shown in 4 ms increments, with the transient crater formed at about 44 ms (11 time steps). The plume profiles in the bottom panel are shown in 2 ms increments, with the transient crater formed at 45 ms (23 time steps). Note the change in plume profile from concave to convex as the final crater rim is passed, along with a noticeable change in velocity with position – rapidly slowing as the final rim is approached and gaining speed again as the slower particles fall out first. Compare these figures to the more basic Figure 5.
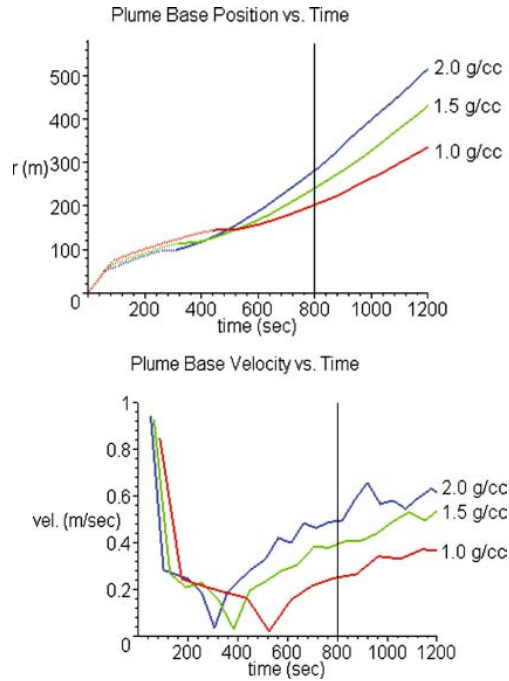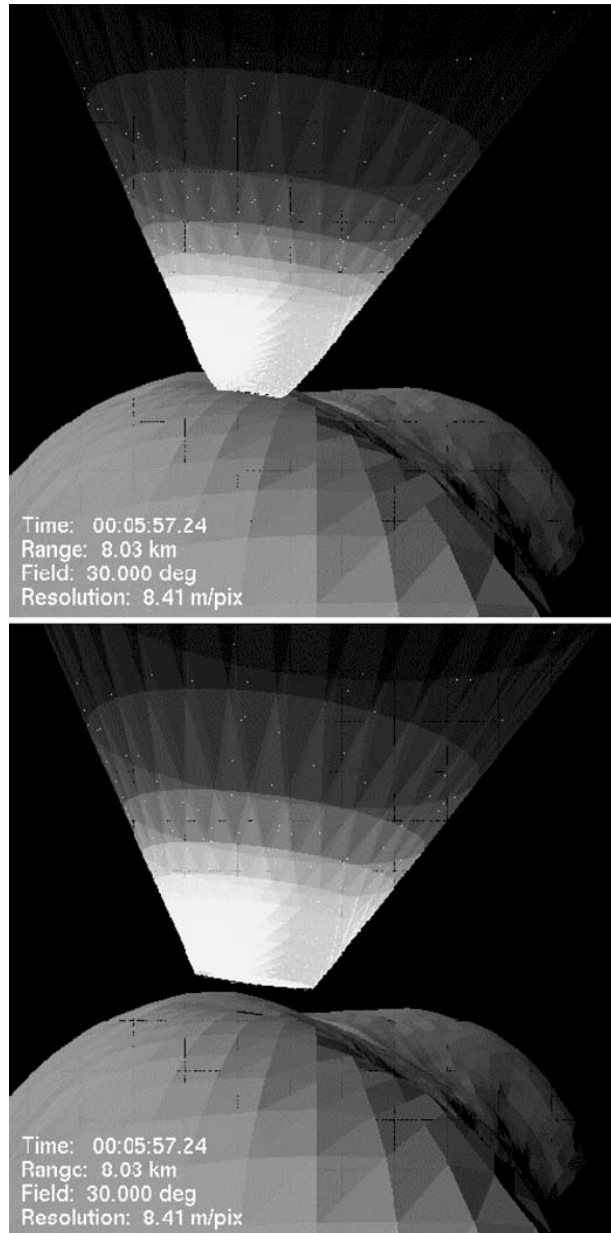
Plume Base Position vs. Time

Plume Base Velocity vs. Time

Figure 9. Plots of model ejecta plume position as a function of time (A) and ejecta plume velocity as a function of time (B) for three different assigned densities to a homogeneous, ellipsoidal comet shape-model: 1.0 g/cm³ *red*, 1.5 g/cm³ *green*, and 2.0 g/cm³ *blue*. Dotted portions of the lines in the upper figure indicate the excavation (plume formation) stage, while the solid portions show the plume fall-out stage. The vertical black line at 800 s indicates the limit of observation time for the Deep Impact mission. Note the different expansion rates as a function of comet gravity, particularly evident in the velocity curves. The velocity curves also display a noticeable decrease in velocity during crater formation, an inflection point at the crater formation time t_{f}, and increasing velocity as slower particles fall out. With good ejecta plume resolution, we plan to use this type of plume behavior to estimate the gravity and mass the comet Tempel 1.

6.4. EJECTA PLUME POLYGON MODEL

A more realistic method for simulating the physical properties of an ejecta plume and eventual blanket resulting from an impact on a small, irregular target body is to model the ejecta plume as a 3D polygon object rather than randomly generated tracer particles. At each time step, the surface area and opacity of each polygon of the ejecta plume is calculated and rendered appropriately (assuming a user-specified particle distribution). Figure 10 shows an example of this model variant, for both a gravity-dominated and strength-dominated cratering event.

Time: 00:05:57.24
Range: 8.03 km
Field: 30.000 deg
Resolution: 8.41 m/pix

Time: 00:05:57.24
Range: 8.03 km
Field: 30.000 deg
Resolution: 8.41 m/pix

The polygon ejecta plume is initially formed by placing a mesh of 1,800 regularly spaced tracer particles on the starting surface area of the crater, such that 3,540 roughly equal-area triangular polygons are formed (each formed by connecting three tracer particles). This creates 59 rings of 60 polygons each, ranging from Sqrt((1/60) * R^2) to R in radius – the hole in the center is intentional, in order to avoid the region of very fast ejecta particles which produce extremely deformed polygons and do not contribute significantly to the visible ejecta plume.

We currently calculate the mass of impact ejecta that each polygon represents by dividing the excavated portion of the crater into a series of simple paraboloid shells. The mass of material injected into each ring of 60 polygons is given by:

$$m_i = \frac{\rho_t \pi}{8} \left(r_{i+1}^3 - r_i^3 \right), \tag{15}$$

where m_i is the mass injected in ring i. The mass per polygon in this ring is thus $m_0 = (1/60)m_i$. This estimate is based on the assumption that the excavation depth of the transient crater is about $D/8$ or $R/4$ (Melosh, 1989). The initial mass loading per polygon will remain constant throughout the simulation, while the surface area of the polygon A will change dramatically throughout ejection and flight. Along with the target surface density ρ_t (which is also used as a particle density), the user must supply a mass distribution description, consisting of the smallest and largest particle diameters – which are converted to a minimum and maximum particle mass – and a cumulative distribution power-law exponent. This is described by:

$$dN = K m_p^{-b} dm_p, \tag{16}$$

where N is the cumulative number of particles, K is a constant, m_p is the particle mass, and b the supplied power-law exponent.

This gives us a means to derive the optical scattering properties of each ejecta plume polygon, which is a function of the scattering properties of each individual particle's surface area and albedo. The surface area of an individual particle is given by:

$$a = \pi \left(\frac{3m_p}{4\pi \rho_t} \right)^{2/3}. \tag{17}$$

Figure 10. A simulation showing the ejecta plume as a 3D shape-model for a small gravity-dominated cratering event (*top*) and a small strength-dominated cratering event (*bottom*) on an Eros-shaped target body. An ejecta particle size distribution has been assumed (maximum particle size, minimum particle size, and power-law distribution) with the resulting ejecta plume opacity calculated and rendered. Note that the ejecta plume detaches from the target body in the case of (*bottom*) strength-dominated cratering, with the first particles landing on the surface again at some distance from the impact crater site (if they do at all). In both simulations, a few random ejecta blocks are also included as discrete points. In the (*top*) gravity-dominated event, the convex shape of the ejecta plume indicates that the transient crater has finished forming and that the ejecta plume is now in the fall-out stage.

The total surface area per unit volume σ_v is found by solving $d\sigma_v = a\, dN$, which yields:

$$\sigma_v = \pi \left(\frac{3}{4\pi\rho_t} \right)^{2/3} \left(\frac{K}{(5/3) - b} \right) \left(m_l^{(5/3)-b} - m_s^{(5/3)-b} \right), \tag{18}$$

where m_l and m_s are the mass of the largest and smallest particles, respectively. We place the constant K in terms of the mass density within the plume ρ_e, by solving $d\rho_e = m_p\, dN$:

$$\rho_e = \left(\frac{K}{2 - b} \right) \left(m_l^{2-b} - m_s^{2-b} \right), \tag{19}$$

Solving this expression for K, substituting back into the expression for σ_v, and re-arranging to find the surface area per unit mass σ_m gives:

$$\sigma_m = \frac{\sigma_v}{\rho_e} = \pi \left(\frac{3}{4\pi\rho_t} \right)^{2/3} \left(\frac{2 - b}{(5/3) - b} \right) \left(\frac{m_l^{(5/3)-b} - m_s^{(5/3)-b}}{m_l^{2-b} - m_s^{2-b}} \right), \tag{20}$$

which is an intrinsic property of the ejecta plume, based on the user supplied mass distribution of particles.

To determine the opacity of individual ejecta plume polygons as a function of their changing surface areas A, we make use of the *Lambart Exponential Absorption Law* (Chamberlain and Hunten, 1987):

$$I_f = I_0\, e^{-\sigma_m \psi}, \tag{21}$$

where I_0 is the initial light intensity, I_f the final light intensity, and ψ the mass loading per unit area within the plume polygon ($\psi = m_0/A$). Note that $\sigma_m \psi$ is equivalent to the optical depth of the plume. Normalizing the light intensity and bringing in the change in polygon area over the course of the simulation gives an opacity O equation for each polygon:

$$O = 1 - e^{-\sigma_m \psi_0 (A_0/A)}, \tag{22}$$

where ψ_0 and A_0 are the initial mass per unit area and initial polygon area, respectively. Note that this opacity applies to viewing the plume surface from a normal (perpendicular) direction, and does not yet take into account the variable albedo of the particles to different light wavelengths. These inputs are supplied to a rendering tool (the *OpenGL* package), for visualization.

For our current modeling purposes, we use mass distribution values from a typical comet dust environment (Lisse *et al.*, 2004) for the ejecta plume, although we expect that the actual observed plume will have a coarser particle distribution (and be correspondingly less opaque). When the actual observations are made, parameter searches using this forward model will be performed to better constrain these ejecta plume properties.

6.5. Instrument Image Sequence Simulations

We also used this final form of the ejecta plume model in the planning of the instrument image sequences for the comet flyby spacecraft. This is done by modeling
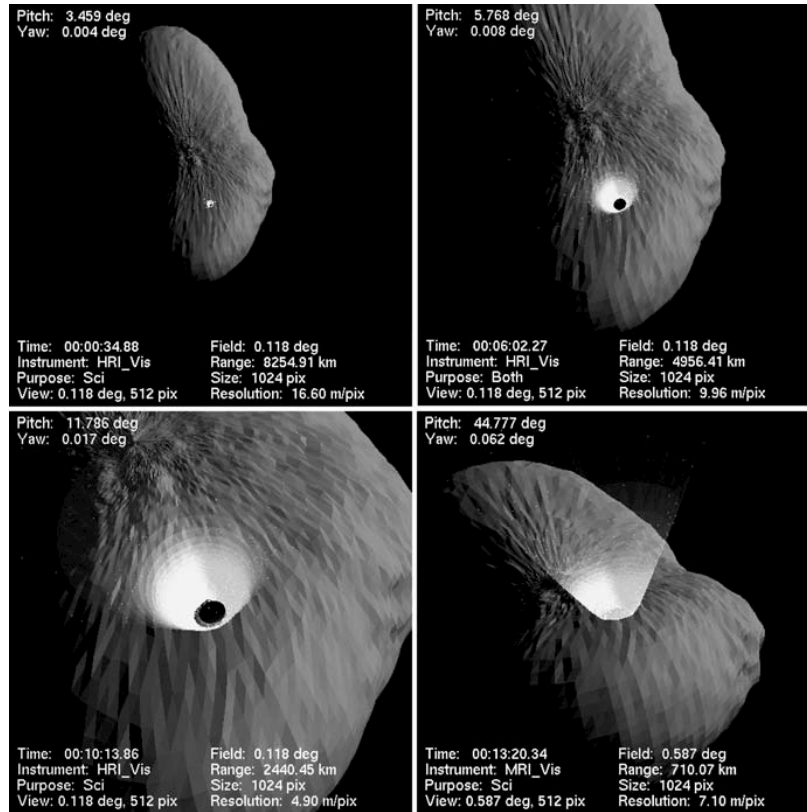

Figure 11. A few sample images from an instrument sequence simulation for the Deep Impact mission High-Resolution Instrument (HRI), showing false color renderings of a modified-Borelly comet shape-model *grey*, transient crater surface area *black*, ejecta plume *white*, and several hundred random ejecta fragments *white*. The first image (*upper left*) shows the view about 30 s after impact, showing the forming crater and ejecta plume. The second image (*upper right*) shows the view shortly after transient crater formation is complete. The third image (*lower left*) shows what some of our best views of the interior of the crater might look like as the point of closest approach is rapidly passed. The fourth image (*lower right*) shows the last possible image of the comet and ejecta plume as seen by the Medium-Resolution Instrument (MRI) just before putting the spacecraft in Safe Mode at closest approach. This sequence depicts one of our best possible scenarios: with a comet presenting a large face-on profile, an excellent hit by the impactor, a well-behaved gravity-dominated cratering event, very little image smear, and excellent impact site tracking for instrument pointing. What we actually see will most likely not be this ideal!

an impact on a shape-model target body and viewing it through a specifically designed display module that simulates the flight path of the comet and flyby spacecraft, comet orientation and sunlight, spacecraft orientation, and instrument field-of-view and mode information (Figure 11). This image sequence modeling can also be used after the actual encounter to forward model many of the observed features from the impact and flyby.

7. Conclusion

Impact cratering theory and modeling play an important role in the Deep Impact mission, from initial inception to final data analysis. Experimentally derived impact crater scaling laws provide us with our best estimates for the crater diameter, depth, and formation time. Cratering theory has strongly influenced the impactor design, producing a craft that should produce the largest possible crater on the surface of Tempel 1 under a wide range of scenarios. Numerical hydrocode modeling allows us to estimate the volume and thermodynamic characteristics of the material vaporized in the early stages of the impact (a mixture of impactor and comet material) with a view towards disentangling these two components when the actual impact occurs. Hydrocode modeling will also aid us in understanding the observed crater excavation process, especially in the area of impacts into porous materials. Finally, experimentally derived ejecta scaling laws and modeling provide us with a means to predict and analyze the observed behavior of the material launched from the comet during crater excavation, and may provide us with a unique means of estimating the magnitude of the comet's gravity field and by extension the mass and density of comet Tempel 1. Together with laboratory cratering experiments (Schultz and Ernst, this volume), impact cratering theory and computational modeling will provide us with important tools toward understanding the results of this unique impact experiment on comet Tempel 1.

References

Anderson, C. E.: 1987, *Int. J. Impact Eng.* **5**, 33.

Anderson, J. L. B., Schultz, P. H., and Heineck, J. T.: 2003, *J. Geophys. Res. (Planets)* **108**, 13.

Artemieva, N. A. and Ivanov, B. A.: 2001, *Lunar Planet. Inst. Conf. Abst.* **32**, 1431.

Asphaug, E. and Benz, W.: 1994, *Nature* **370**, 120.

Brandt, J. C. and Chapman, R. D.: 2004, *Introduction to Comets*, Cambridge University Press, Cambridge, USA.

Brownlee, D. E., Horz, F., Newburn, R. L., Zolensky, M., Duxbury, T. C., Sandford, S., *et al.*: 2004, *Science* **304**, 1764.

Chamberlain, J. W. and Hunten, D. M.: 1987, *Theory of Planetary Atmospheres*, Academic Press, San Diego.

Cintala, M. J., Berthoud, L., and Hörz, F.: 1999, *Meteor. Planet. Sci.* 34, 605.

Collins, G. C., Melosh, H. J., and Ivanov, B. A.: 2004, *Meteor. Planet. Sci.* **39**, 217.

Croft, S. K.: 1981, in Schultz, P. H. and Merrill, R. B. (eds.), *Multi-Ring Basins*, Pergamon Press, New York, p. 207.

Geissler, P., Petit, J. M., Durda, D. D., Greenberg, R., Bottke, W. F., and Nolan, M. C.: 1996, *Icarus* **120**, 140.

Grady, D. E. and Kipp, M. E.: 1987, in Atkinson, B. K. (ed.), *Fracture Mechanics of Rock*, Academic Press, San Diego, p. 429.

Heiken, G. H., Vaniman, D. T., and French, B. M.: 1991, *Lunar Sourcebook*, Cambridge University Press, Cambridge, USA.

Holsapple, K. A.: 1980, *Lunar and Planetary Science Conference*, Vol. 11, Pergamon Press, New York, p. 2379.

Holsapple, K. A. and Schmidt, R. M.: 1982, *J. Geophys. Res.* **87**, 1849.

Housen, K. R., Schmidt, R. M., and Holsapple, K.A.: 1983, *J. Geophys. Res*. **88**, 2485.

Jessberger, E. K.: 1999, *Space Sci. Rev.* **90**, 91.

Larson, D. B.: 1977, *The Relationship of Rock Properties to Explosive Energy Coupling*, UCRL-52204, University of California Research Labs.

Lisse, C. M., A'Hearn, M. F., Fernandez, Y. R., McLaughlin, S. A., Meech, K. J., and Walker, R. J.: 2004, *Icarus*, in press.

Love, S. G., Hörz, F., and Brownlee, D. E.: 1993, *Icarus* **105**, 216.

McGlaun, J. M., Thompson, S. I., and Elrick, M. G.: 1990, *Int. J. Impact Eng.* **10**, 351.

Melosh, H. J.: 1989, *Impact Cratering: A Geologic Process*, Oxford University Press, New York.

Melosh, H. J.: 2000, *Lunar Planet. Inst. Conf. Abst.* **31**, 1903.

Melosh, H. J. and Ivanov, B. A.: 1999, *Ann. Rev. Earth Planet. Sci.* **27**, 385.

Nolan, M. C., Asphaug, E., Melosh, H. J., and Greenberg, R.: 1996, *Icarus* **124**, 359.

Nordyke, M. D.: 1962, *J. Geophy. Res.* **67**, 1965.

Peale, S. J.: 1989, *Icarus* **82**, 36.

Pierazzo, E., Artemieva, N. A., and Spitale, J. N.: 2001, *ESF-IMPACT 5: Catastrophic Events and Mass Extinctions: Impacts and Beyond*, Granada, Spain.

Poorman, K. L. and Piekutowski, A. J.: 1995, *Int. J. Impact Eng.* **17**, 639.

Rubin, M. B., Vorobiev, O. Y., and Glenn, L. A.: 2000, *Int. J. Solids Struc.* **37**, 1841.

Sagdeev, R. Z., Elyasberg, P. E., and Moroz, V. I.: 1988, *Nature* **331**, 240.

Scotti, J. and Melosh, H. J.: 1993, *Nature* **365**, 733.

Schmidt, R. M. and Housen, K. R.: 1987, *Int. J. Impact Eng.* **5**, 543.

Schultz, P. H. Anderson, J. L. B., and Heineck, J. T.: 2002, *Lunar Planet. Inst. Conf. Abst.* **33**, 1875.

Schultz, P. H. and Ernst, C.: 2005, *Space Sci. Rev.*, this volume.

Shuvalov, V. V.: 1999, *Shock Waves* **9**, 381.

Taylor, S. R.: 1982, *Planetary Science: A Lunar Perspective*, Lunar and Planetary Institute, Texas.

Thompson, S. L. and Lauson, H. S.: 1972, *Improvements in the Chart-D radiation hydrodynamic code III: Revised analytical equation of state*, Sandia National Laboratories Report SC-RR-710714, Albuquerque, New Mexico, 119 pp.

Werner, R. A.: 1994, *Celest. Mech. Dyn. Astron.* **59**, 253.

Wroth, C. P. and Bassett, R. H.: 1983, G*éotechnique* **33**, 32.

Wünnemann, K. and Ivanov, B. A.: 2003, *Planet. Space Sci.* **51**, 831.